Published in final edited form as:

ACS Appl Mater Interfaces. 2017 May 17; 9(19): 16725–16733. doi:10.1021/acsami.7b04881.

High-Resolution Bubble Printing of Quantum Dots

Bharath Bangalore Rajeeva[†,‖], **Linhan Lin**[†,‖], **Evan P. Perillo**[‡], **Xiaolei Peng**[†], **William W. Yu**[§], **Andrew K Dunn**[‡], and **Yuebing Zheng**[*,†]

[†]Materials Science and Engineering Program, Department of Mechanical Engineering and [‡]Department of Biomedical Engineering, The University of Texas at Austin, Austin, Texas 78712, United States [§]Department of Chemistry and Physics, Louisiana State University, Shreveport, Louisiana 71115, United States

Abstract

Semiconductor quantum dots (QDs) feature excellent properties, such as high quantum efficiency, tunable emission frequency, and good fluorescence stability. Incorporation of QDs into new devices relies upon high-resolution and high-throughput patterning techniques. Herein, we report a new printing technique known as bubble printing (BP), which exploits a light-generated microbubble at the interface of colloidal QD solution and a substrate to directly write QDs into arbitrary patterns. With the uniform plasmonic hot spot distribution for high bubble stability and the optimum light-scanning parameters, we have achieved full-color QD printing with submicron resolution (650 nm), high throughput (scanning rate of ~10^{-2} m/s), and high adhesion of the QDs to the substrates. The printing parameters can be optimized to further control the fluorescence properties of the patterned QDs, such as emission wavelength and lifetime. The patterning of QDs on flexible substrates further demonstrates the wide applicability of this new technique. Thus, BP technique addresses the barrier of achieving a widely applicable, high-throughput and user-friendly patterning technique in the submicrometer regime, along with simultaneous fluorescence modification capability.

Graphical abstract

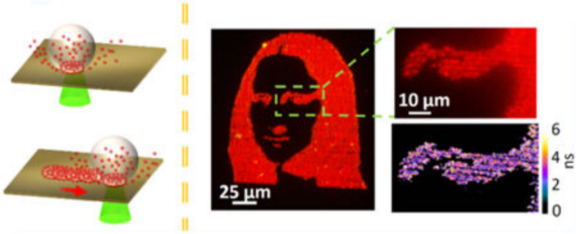

---

[*]Corresponding Author: zheng@austin.utexas.edu.

[‖]**Author Contributions**: B.B.R. and L.L. contributed equally to this work.

Orcid: William W. Yu: 0000-0001-5354-6718
Yuebing Zheng: 0000-0002-9168-9477

Supporting Information: The Supporting Information is available free of charge on the ACS Publications website at DOI: 10.1021/acsami.7b04881.

Notes: The authors declare no competing financial interest.

Keywords

bubble printing; high-resolution printing; quantum dots; direct-write; fluorescence modification

Introduction

With strong quantum confinement effect, high crystal quality and precisely controllable size, chemically synthesized semiconductor quantum dots (QDs) show their advantages over organic luminescence materials, such as tunable absorption and emission wavelength, narrow emission bandwidth, high quantum efficiency, and excellent stability.[1–4] Typical QD applications include light-emitting devices,[5] information displays,[6] photovoltaics,[7] biosensing,[8] nanolasers,[9] and photo-detectors.[10,11] The optical performance of QDs can be further enhanced by placing the QDs at plasmonic substrates,[12] which can significantly improve the spontaneous emission rate by the Purcell effect and modify the emission direction by coupling the emitted photon into directional scattering light.[13,14] The plasmon–QD hybrid systems can enhance many of the applications, including full-color displays and nanolaser.[15]

However, the translation of QDs into the above-mentioned real-life applications relies on the capability to pattern or print QDs from solutions onto the predetermined locations of solid-state substrates.[16,17] In particular, the realization of applications in photonics and biotechnology highly depends on the structured patterning of QDs. To this end, the major approaches explored include Langmuir–Blodgett (LB) print-ing,[18,19] microtransfer printing,[6] intaglio printing,[20] gravure printing,[21] inkjet printing,[22] and electrohydrodynamic jet (E-Jet) printing.[23] The mask-based approaches (i.e., LB printing, transfer printing, and intaglio printing) have shown promise of achieving extremely high-resolution patterning down to single-QD level.[18] In contrast, ink/nozzle-based printing techniques (i.e., inkjet and E-Jet) are direct-writing approaches, which circumvent the reliance on a mask and thus reduce the overhead cost considerably. However, it has remained challenging to manufacture complex structures at submicrometer resolution because of inherent technological barriers, such as the spreading of the ink upon exposure to the substrate and long postprocessing time for the inks to dry.[22] Therefore, developing a broadly applicable, high-resolution, and precise printing technique is critical for the widespread applications of the semiconductor QDs.

Herein, we exploit a light-directed microbubble to capture and print QDs in their native liquid environments, which is termed as bubble printing (BP). By generating and translating optothermally generated mesobubbles (bubble with a diameter of <1 μm) on a plasmonic substrate, we are able to rapidly deliver the suspended QDs toward the air–liquid interface by Marangoni convection and to immobilize the QDs on the plasmonic substrates with precise site control. Our BP technique addresses a major technical challenge regarding the development of a versatile printing technique with a resolution of <1 μm.[22] It offers versatility of achieving complex morphologies with extremely low material wastage, high throughput (maximum scanning rate of ~10^{-2} m/s), high resolution (~650 nm), and real-time configurable patterning. By controlling the optical power for bubble control, we further modify fluorescence wavelength and lifetime of the printed QDs. To further demonstrate the versatility, we achieve BP patterning of QDs on flexible substrates, which enables multiple applications, such as flexible displays,[24] optoelectronic circuits,[25] and sensors.[26] With the high resolution, high throughput, real-time reconfigurable operation, and modification capability of QD fluorescence, BP will advance the applications of semiconductor QDs in nanoelectronics and nanophotonics.

■ Experimental Section

QDs

In general, water-soluble QDs with emission colors of red (615 nm), yellow (585 nm), and green (520 nm) were synthesized using a recently reported method.[27] Briefly, QDs with CdSe/CdS core/shell structures were synthesized at the CdS shell growth temperature of 180 °C.[28] The core/shell QDs were purified and stored in chloroform. QD concentrations were determined using the extinction coefficients.[29,30] Poly(maleic anhydride-*alt*-1-octadecene) (PMAO, M_n = 30 000–50 000, Aldrich) reacted with amino poly(ethylene glycol) methyl ether (mPEG-NH_2, MW 6000) in chloroform overnight (room temperature) to form an amphiphilic polymer (PMAO-PEG) (molar ratio of PMAO/PEG was 1:10). The QDs and PMAO-PEG were mixed in chloroform and stirred for 1 h at room temperature (molar ratio of QD/PMAO-PEG was 1:10). Water with the same volume of the chloroform was added, and the latter was gradually removed by rotary evaporation at room temperature, leading to a clear and colored solution of water-soluble QDs. An ultra-centrifuge (Beckman Coulter Optima L-80XP) was used to further concentrate and purify (i.e., removing excessive amphiphilic polymer) the materials (typically at 200 000–300 000 g for 1–2 h).

Plasmonic Substrates

To prepare the plasmonic substrates, a 4 nm Au film was deposited on a glass substrate by thermal deposition (Denton thermal evaporator) at a base pressure of 9×10^{-6} Torr. The sample was subsequently annealed at 550 °C for 2 h. To prepare a flexible substrate, a poly(ethylene terephthalate) (PET) film was initially attached on a glass slide and a 4 nm Au film was deposited onto the PET film using the same thermal deposition parameters stated above. The Au thin film on PET film without the annealing process was used as flexible substrate for BP.

BP

The BP process was performed by a combination of the stage translation and shutter activation/deactivation. The printing process was monitored in real time through a charge-coupled device with a white-light source illuminating the substrate from the top. A Prior ProScan Scientific stage with an x–y resolution of 14 nm was used, along with a motorized flipper (Thorlabs MFF102) that acted as a shutter. The response time of the flipper is 500 ms. The stage and shutter integrated with the optical path were synchronously controlled with a custom-written LabVIEW code. The code also controlled the stage-translation speed. The stage moved along the predetermined (x, y) coordinates with an on/off status of the shutter for each coordinate. A MATLAB script was used to obtain the coordinates and the shutter status from a stencil of the desired pattern.

Scanning Electron Microscopy (SEM) and Atomic Force Microscopy (AFM) Characterization

SEM images were obtained using the FEI Quanta 650 ESEM. AFM images were taken with Park Scientific AFM under the noncontact mode.

Optical Characterizations

A Zeiss LSM 710 microscope was used for wide-field fluorescence imaging. Unless mentioned otherwise, the imaging was performed with a 405 nm excitation source and without any emission filters. The composite images were generated via wavelength-dependent coloring feature in the Zeiss ZEN software. The fluorescence lifetime imaging (FLIM) of the QDs was done via time-correlated single-photon counting (TCSPC), with a femtosecond titanium:sapphire laser modified to 800 nm (~200 fs) (Mira 900; Coherent), galvo scanning mirrors (6215H; Cambridge Tech.), and a GaAsP photomultiplier tube (PMT) (H7422PA-40; Hamamatsu) in nondescanned detection scheme. The output current of the PMT was amplified using a preamplifier with 2 GHz cutoff (HFAC- 26; Becker & Hickl GmbH). The amplified pulses from the PMTs were sent to the TCSPC module (SPC-150; Becker & Hickl GmbH). The objective was a silicone oil immersion lens with a numerical aperture of 1.3 (UPLSAPO60X; Olympus). Using an average laser power of 1 mW, fluorescence lifetimes were recorded with a 20 ps time resolution and a pixel integration time of 5 ms. The lifetime fitting was done with the least-squares method using a model of a single exponential decay convolved with a Gaussian impulse function. The resultant lifetime image was threshold based on intensity to remove the background signals from the plasmonic substrate. To ensure a high fitting quality, data points with less than 500 photons were removed from the fitting, and the fittings with $\chi^2 < 2$ were discarded.

Results and Discussion

Figure 1a shows the schematic of optical setup for BP. The aqueous QD solution is confined between a plasmonic substrate consisting of gold nanoparticles (AuNPs) (see Experimental Section for details) and a glass coverslip with a 500 μm thick spacer. Upon irradiation of a continuous-wave laser beam (532 nm) through a high-magnification objective, the AuNPs excited on resonance reemit the energy via nonradiative Landau damping, which results in an elevated temperature over the AuNP surfaces (Figure 1b).[31–33] This plasmon-enhanced photothermal heating causes overheating and leads to the formation of the mesobubble,[34] whose diameter can be controlled from submicron to micron regimes by tuning the optical power. The temperature gradient along the bubble surface causes the Marangoni convection and therefore the delivery of QDs toward the bubble surface by convective drag force. The QDs are trapped at the bubble–liquid interface with a force balance of the gas–liquid pressure difference, the drag force, and the surface tension.[35-38] The QDs are eventually immobilized on the substrate by the van der Waals interaction between QDs and plasmonic substrate and the thermal heating. When the bubble is translated over the substrate via deflection (movement of laser beam controlled by spatial light modulator) or displacement (stage movement) techniques, the QDs are patterned along the path traversed by the laser beam (Figure 1c). In the present case, we achieve large-area versatile patterning of QDs via stage translation.

Because the bubble is created on the basis of the plasmon-enhanced optothermal heating of the plasmonic substrate, the uniformity of the AuNPs and their constituent “hot spots” on our substrate (Figures S1 and S2) ensures the light-directed bubble generation at any arbitrary location. Upon bubble generation, a constant temperature increase at each instance is mandated to maintain a consistent bubble size. In general, the total temperature change (ΔT_{total}) can be considered as a combination of increase in temperature of a single AuNP (ΔT_{np}: self-contribution due to optical absorption) and the external contribution from the surrounding AuNPs (ΔT_{ext}), which leads to $\Delta T_{\text{total}} = \Delta T_{\text{np}} + \Delta T_{\text{ext}}$. The ratio of the self to external components can be estimated by considering the particle radius (R), interparticle separation (p), and full width at half-maximum (FWHM) of the Gaussian laser beam (L) according to eq 1[39]

$$\frac{\Delta T_{\text{np}}}{\Delta T_{\text{ext}}}=\frac{p^2}{3\text{LR}} \quad (1)$$

From the SEM image, we estimate the average AuNP radius and interparticle distance to be 30 and 15 nm, respectively. Assuming a value of 500 nm for FWHM, the ratio is found to be 3×10^{-3}. This implies that the temperature increase is in the delocalized regime and is a cumulative effect of particles exposed to the laser. A random area selection over the plasmonic substrate (Figure S1) establishes the uniformity of AuNP distribution in terms of area coverage, with a standard deviation of 0.54%. The highly uniform AuNP density along with the delocalized photothermal conversion ensures that a constant temperature is produced throughout the substrate, enabling the generation of bubbles with a uniform size.

The precise control of QD patterns in BP requires a stable translation of the photothermally generated bubble along a preset trajectory. The translation is governed by a steady-state process, where the photothermal heat on the AuNPs is balanced by the thermal loss from the bubble to the surrounding liquid at room temperature. The thermal analysis of plasmonic substrates has been analyzed in prior works, which revealed the photothermal energy radially propagating outward from the laser beam spot. [40,41] Treating the bubble as a sphere, we can estimate the outward heat flux from the bubble using Fourier's law

$$\frac{\mathrm{d}Q}{\mathrm{d}T}=4\pi k R^2 \partial_{\mathrm{r}} T \quad (2)$$

where Q is the heat power of the incident laser (J), k is the thermal conductivity of water (J s^{-1} m^{-1} K^{-1}), R is the radius of the bubble (m), T is the temperature (K), and $\partial_{\mathrm{r}} T$ is the temperature gradient at the edge of the bubble (K/m). By assuming $\partial_{\mathrm{r}} T \approx \frac{\Delta T}{R}$, where ΔT is the temperature difference across the bubble surface (Figure 1d), we get

$$\frac{\mathrm{d}Q}{\mathrm{d}T}=4\pi kR\Delta T \qquad (3)$$

With the assumption that temperature difference ΔT remains the same under similar illumination conditions, the steady-state thermal loss is proportional to R.[42] In other words, a smaller bubble can retain the steady state for a longer period due to lower thermal loss. In addition to the lower heat loss, the minimal air concentration within the bubble helps maintain the stability of the mesobubble (bubble diameter <1 μm). It is noted that the highly focused laser beam and plasmonic substrate with uniform high-density AuNPs effectively reduce the size of the light-generated bubble for the stable BP of QDs. In the present study, we apply BP to pattern colloidal CdSe/ CdS QDs encapsulated with an amphiphilic coating and dispersed in an aqueous medium. Various QDs with emission colors of red, yellow, and green (see Experimental Section for details) were used by adding ~50 μL droplets of the solutions over the plasmonic substrates. On the basis of the analysis of the video frames, we found that the mesobubble dissolution (upon laser switch-off) time is in the range of 250–300 ms. For the submicron bubble, the concentration of air molecules within the bubble is limited, and the bubble is mostly composed of water vapor, which ensures extremely fast disappearance of the bubble upon the laser switch-off (Figure S3) in contrast to air bubbles, which can last from several seconds to hours.[43] The quick transition between on and off states of the bubble is necessary for high-speed patterning. Further reduction in the dissolution time can be potentially achieved by generating smaller bubbles via utilization of highly confined hot spots to realize stronger thermal gradient (e.g., bow-tie antenna array).[33,39] An alternate strategy could be the utilization of degassed water to reduce the two-way mass transfer between vapor bubble and dissolved gas in the solvent, thereby leading to the faster bubble dissolution.[44]

A precise control over the line width of the QD pattern is critical for advanced applications. For continuous patterning, the relationship between the incident laser intensity and the pattern line width was examined (Figure 2a). With an increase in the optical power, the bubble size increases due to the generation of a higher amount of vapor. A linear regression line was obtained from the plot of pattern line width and the incident laser power, demonstrating the ease of modulating the patterns by the laser power. The lowest line width of <700 nm (Figure S4) is observed at an incident power intensity of 0.28 mW/μm^2. Increasing power also changes the QD pattern morphology from scalloped lines to lines with uneven line width, eventually leading to individual bubble geometry. Further increase in the optical power causes the coalescence of adjacent bubbles into larger bubbles, which are not suitable for BP because of long bubble lifetime. Figure S5 shows a bright-field image of three types of large-area rectangular patterns of QDs fabricated via raster scanning of laser beam, which demonstrates the tunability of the QD pattern density by line spacing (i.e., 1, 1.5, and 2 μm). Further, by using a stage wait time of 500 ms and 1 μm stage steps, crowding of the QDs at the edge of each bubble can be achieved. This creates a pattern resembling arrays of QD clusters as individual pixels. We observed an average FWHM of 400 nm for the pixels with a high-resolution two-photon fluorescence microscope (Figure S6).

Following process parameter optimization, we have demonstrated the versatility of BP in Figure 2. Initially, the QDs were bubble-printed along a contour by programmed translation of the sample stage. Figure 2b shows the microscale patterning of red QDs in the shape of a butterfly. It is worth noting that the head of the butterfly that involves closely spaced circles of diameter ~8 μm is precisely patterned without any spreading, bubble coalescence, or distortion. With short dissolution and generation times of the mesobubble, it is also possible to create more complicated patterns at high resolution and speed. Figure 2c,d shows the high-resolution intricate patterns of red QDs resembling famous personalities, such as Charlie Chaplin and Mona Lisa, with dimensions of 120 μm × 90 μm and 150 μm × 90 μm, respectively. The magnified image in Figure 2f demonstrates the defining strength of BP, wherein 1 μm gap between adjacent structures (eyebrow and eye) can be realized. To alleviate concerns of fluorescence image saturation, a fluorescence lifetime image of the same region was taken with FLIM microscopy, which demonstrates uniform deposition of QDs within the pattern. The average and root-mean-square (rms) surface roughnesses over the 40 μm × 80 μm region are 12.6 and 16.5 nm, respectively (Figure S7a). The printed red QDs show similar emission characteristics to those of pristine QDs (Figure S7d). A 3.9 nm increase in FWHM can be attributed to the aggregation of QDs.[45] Further, we have demonstrated the capability of BP in fabricating functional luminescent devices in the area of anticounterfeiting technology.[22] Specifically, high-resolution microscale QR codes are desirable for preventing the forging of IC chips.[46] Using BP, a microscale QR code of 80 μm × 80 μm was fabricated. The complicated QR code was achieved by performing a raster scan of green QDs using the laser beam in conjunction with a shutter to determine an on/off state of the printing. In this work, patterns with blue emission were obtained by controlled oxidation of either green or yellow QDs.

Because the patterning process is primarily mediated by the Marangoni convection and subsequent van der Waals interaction, the BP technique is applicable to QDs of variable sizes, shapes, and compositions, which is critical to the fabrication of various devices. We have demonstrated the BP of QDs with different emission colors onto the plasmonic substrates. The same mechanisms for bubble generation (Figure S8), QD entrapment and QD immobilization on the substrates, apply to all types of the QDs. The pattern of Mona Lisa with 1 μm line spacing was replicated with yellow QDs at a high stage-translation speed of 10^{-2} m/s (Figure S9, Video 1). The left panel in Figure 3a shows high-density BP of three types of QDs that emit red, yellow, and blue lights, revealing the potential for printing full-color QD displays.[47] Similar to the QR code scenario, the blue emission was obtained via controlled oxidation of green QDs. The right-hand side panel in Figure 3a shows the corresponding fluorescence spectra of the patterns. For an initial demonstration of multicolor printing, we have shown the regioselective printing of individual red/green/blue emission patterns onto a single substrate. Figure 3b shows the fluorescence image (405 nm excitation) of a bubble-printed contour of U.S. map along with the states of Texas, California, and Pennsylvania. This map was achieved by a multistep printing process, where cross-markers were created (also by BP) for alignment, and a rigorous washing step with isopropyl alcohol and water between each step was applied to remove loosely adsorbed QDs on the substrate. There is strong adhesion of the printed QDs on the plasmonic substrates. For instance, the printed QDs could not be transferred from the substrates to a very sticky

PDMS substrate (30:1; prepolymer/ curing agent), which in turn corresponds to an adhesion strength greater than 6 J m^{-2}.[48] This strong adhesion can be attributed to the convection and the thermal heating effects, and it reduces the ligand length and thereby the QD–substrate separation to yield stronger van der Waals forces.

We have further applied BP to pattern QDs on flexible and bendable plastic substrates. A flexible PET substrate with a 4 nm Au thin film on the surface was utilized for the demonstration. Figure 4a shows the fluorescence image of a longhorn symbol created via BP of red QDs on the PET film. Figure 4b shows a magnified bright-field image of partial longhorn symbol with the PET film mechanically bent, which exhibits the structural integrity of the printed QD pattern under the bent state. Repeating the mechanical bending and recovery of the film for 20 times, as shown in Figure 4c,d, yielded no significant changes in the structural and optical properties of the pattern. In addition, BP on flexible substrates can achieve a similar submicron resolution to that of the rigid substrates (Figure S10a,b). The printed QDs were able to withstand both uniform and nonuniform bending of the substrate due to their strong adhesion to the substrate surface. Therefore, an increase in rms roughness to 35 nm for the PET film (Figure 4e) is not a major barrier toward bubble generation and BP process. In fact, numerous reports on bubble generation consider rms values of >1 μm as rough surfaces.[49]

We have also exploited the BP process to modify the fluorescence characteristics of the patterned QDs on the plasmonic substrates. As shown in Figure 5a, the originally yellow QDs that were bubble-printed into square structures (20 μm × 20 μm) via raster scanning exhibited the variable fluorescence from different BP parameters. From square 1 to square 4, the laser exposure time over QDs increases and the fluorescence wavelength makes a continuous blueshift. The higher incident laser power in conjunction with longer exposure time results in the photon-induced oxidation of the patterned QDs, which causes a spectral shift to shorter wavelengths.[50,51] The formation of the oxide layer reduces the effective diameter of the QDs, thereby increasing the quantum confinement and the band-gap energy. The oxidation effect is evident in the spectrum of square 2, wherein a small shoulder starts to appear at ~525 nm. In this study, the peak wavelength of the patterned QDs can be modified from 591 to 475 nm. The continued oxidation also caused the spectrum to broaden (square 4) (Figure S11).[51]

The use of plasmonic substrates in BP provides another opportunity to modify the optical properties of patterned QDs. To investigate the dynamics of the interactions between the QD excitons and the plasmons at the substrates, we applied time-resolved fluorescence measurements to characterize spontaneous emission rates of QDs under the variable conditions, as shown in Figure 5c. A femtosecond Ti:sapphire laser (800 nm) was used for two-photon excitation of the QDs.[52] The average laser power was 1 mW, corresponding to a relatively low fluence of 7×10^{10} W/cm^2 at the focal point. The shortening of the lifetime of QDs drop-casted on the plasmonic substrates (compared to that of QDs on glass substrates) can be ascribed to the Purcell effect arising from the plasmonic effects.[53] A further reduction in the average lifetime to $\tau_{\text{BP-Au}} = 2.69 \pm 0.29$ ns is observed upon BP of QDs over the plasmonic substrates, which is attributed to the reduced QD–substrate separation due to flow-induced bombardment effect and laser-induced ligand shortening along with QD oxidation.[1,54] We further studied the influence of the printing conditions over the emission rate of the patterned QDs by FLIM on the basis of the setup in Figure S13. Straight lines of QDs were printed with increased incident laser intensity from 0.29 to 0.58 mW/μm^2. The FLIM images were collected by scanning the probing laser beam over the sample area (Figure S13). Figure 5d shows histogram of the lifetimes obtained from each line fabricated at various optical power intensities along with the Gaussian fitting of the lifetime distribution. The lifetime distribution for each power is statistically significant with ~1000 pixels analyzed for each data set (Figure S14). The mean lifetime of the printed patterns increases from 2.26 ns at 0.29 mW/μm^2 to 2.84 ns at the maximum power intensity of 0.58 mW/ μm^2 (Figure 5e). This lifetime increase is due to the larger average separation between QDs and the substrate when the optical power increases the overstacking of the QDs, which is evident in the AFM and optical profilometry images (Figure S13). Further, the lifetime distribution broadens at the higher power due to the higher thickness variations in the lines of QDs. The mean-lifetime modification capability will find applications as an encoding scheme to produce distinguishable optical codes and study biological processes.[55]

■ Conclusions

We have demonstrated BP of QDs for the fabrication of patterned plasmon-QD hybrid structures. The high bubble stability is attributed to the increase of delocalized temperature over uniform AuNPs on the plasmonic substrates. Furthermore, the vapor bubbles with short dissolution times improve BP throughput. BP can simultaneously achieve high resolution (<1 μm line width), high throughput (>10^5 μm/s), and low material usage. The versatile printing capabilities of BP are demonstrated for multicolor QDs on both rigid and flexible substrates. The plasmonic and photothermal effects in the BP can be further exploited to modify the QD emission wavelengths and dynamics via controlled thermal oxidation and plasmon–exciton interactions. With high resolution and throughput, BP will find applications in high-resolution QD display, high-density information storage, and biomedical assays.

Supplementary Material

Refer to Web version on PubMed Central for supplementary material.

Acknowledgments

The authors acknowledge the financial support of the Beckman Young Investigator Program and the Texas Advanced Computing Center (TACC) at The University of Texas at Austin for providing HPC resources that have contributed to the research results reported within this article (URL: http://www.tacc.utexas.edu). They also thank M. Wang and Z. Wu for helpful discussions.

References

1. Pietryga JM, Park YS, Lim JH, Fidler AF, Bae WK, Brovelli S, Klimov VI. Spectroscopic and Device Aspects of Nanocrystal Quantum Dots. Chem Rev. 2016; 116:10513–10622. [PubMed: 27677521]
2. Yin Y, Talapin D. The Chemistry of Functional Nanomaterials. Chem Soc Rev. 2013; 42:2484–2487. [PubMed: 23456089]

3. Yu WW, Peng XG. Formation of High-Quality CdS and Other II-VI Semiconductor Nanocrystals in Noncoordinating Solvents: Tunable Reactivity of Monomers. Angew Chem, Int Ed. 2002; 41:2368–2371.
4. Cassette E, Helle M, Bezdetnaya L, Marchal F, Dubertret B, Pons T. Design of New Quantum Dot Materials for Deep Tissue Infrared Imaging. Adv Drug Delivery Rev. 2013; 65:719–731.
5. Mashford BS, Stevenson M, Popovic Z, Hamilton C, Zhou ZQ, Breen C, Steckel J, Bulovic V, Bawendi M, Coe-Sullivan S, Kazlas PT. High-Efficiency Quantum-Dot Light-Emitting Devices with Enhanced Charge Injection. Nat Photonics. 2013; 7:407–412.
6. Kim TH, Cho KS, Lee EK, Lee SJ, Chae J, Kim JW, Kim DH, Kwon JY, Amaratunga G, Lee SY, Choi BL, Kuk Y, Kim JM, Kim K. Full-Colour Quantum Dot Displays Fabricated by Transfer Printing. Nat Photonics. 2011; 5:176–182.
7. Lan X, Masala S, Sargent EH. Charge-Extraction Strategies for Colloidal Quantum Dot Photovoltaics. Nat Mater. 2014; 13:233–240. [PubMed: 24553652]
8. Medintz IL, Clapp AR, Mattoussi H, Goldman ER, Fisher B, Mauro JM. Self-Assembled Nanoscale Biosensors Based on Quantum Dot FRET Donors. Nat Mater. 2003; 2:630–638. [PubMed: 12942071]
9. Lee AD, Jiang Q, Tang MC, Zhang YY, Seeds AJ, Liu HY. InAs/GaAs Quantum-Dot Lasers Monolithically Grown on Si, Ge, and Ge-on-Si Substrates. IEEE J Sel Top Quantum Electron. 2013; 19 No. 1901107.
10. Konstantatos G, Howard I, Fischer A, Hoogland S, Clifford J, Klem E, Levina L, Sargent EH. Ultrasensitive Solution-Cast Quantum Dot Photodetectors. Nature. 2006; 442:180–183. [PubMed: 16838017]
11. Kagan CR, Lifshitz E, Sargent EH, Talapin DV. Building Devices from Colloidal Quantum Dots. Science. 2016; 353 No. aac5523.
12. Gu H, Zheng RK, Zhang XX, Xu B. Facile One-Pot Synthesis of Bifunctional Heterodimers of Nanoparticles: A Conjugate of Quantum Dot and Magnetic Nanoparticles. J Am Chem Soc. 2004; 126:5664–5665. [PubMed: 15125648]
13. Curto AG, Volpe G, Taminiau TH, Kreuzer MP, Quidant R, van Hulst NF. Unidirectional Emission of a Quantum Dot Coupled to a Nanoantenna. Science. 2010; 329:930–933. [PubMed: 20724630]
14. Hoang TB, Akselrod GM, Mikkelsen MH. Ultrafast Room-Temperature Single Photon Emission from Quantum Dots Coupled to Plasmonic Nanocavities. Nano Lett. 2016; 16:270–275. [PubMed: 26606001]
15. Yang AK, Odom TW. Breakthroughs in Photonics 2014: Advances in Plasmonic Nanolasers. IEEE Photonics J. 2015; 7:1–6.
16. Galatsis K, Wang KL, Ozkan M, Ozkan CS, Huang Y, Chang JP, Monbouquette HG, Chen Y, Nealey P, Botros Y. Patterning and Templating for Nanoelectronics. Adv Mater. 2010; 22:769–778. [PubMed: 20217787]
17. Lan HB, Ding YC. Ordering, Positioning and Uniformity of Quantum Dot Arrays. Nano Today. 2012; 7:94–123.
18. Xie W, Gomes R, Aubert T, Bisschop S, Zhu YP, Hens Z, Brainis E, Van Thourhout D. Nanoscale and Single-Dot Patterning of Colloidal Quantum Dots. Nano Lett. 2015; 15:7481–7487. [PubMed: 26455513]
19. Park JS, Kyhm J, Kim HH, Jeong S, Kang J, Lee SE, Lee KT, Park K, Barange N, Han J, Song JD, Choi WK, Han IK. Alternative Patterning Process for Realization of Large-Area, Full-Color, Active Quantum Dot Display. Nano Lett. 2016; 16:6946–6953. [PubMed: 27733041]
20. Choi MK, Yang J, Kang K, Kim DC, Choi C, Park C, Kim SJ, Chae SI, Kim TH, Kim JH, Hyeon T, Kim DH. Wearable Red-Green-Blue Quantum Dot Light-Emitting Diode Array Using High-Resolution Intaglio Transfer Printing. Nat Commun. 2015; 6 No. 7149.
21. Sun LW, Shi HQ, Li WN, Xiao HM, Fu SY, Cao XZ, Li ZX. Lanthanum-Doped ZnO Quantum Dots with Greatly Enhanced Fluorescent Quantum Yield. J Mater Chem. 2012; 22:8221–8227.
22. Bao B, Li MZ, Li Y, Jiang JK, Gu ZK, Zhang XY, Jiang L, Song YL. Patterning Fluorescent Quantum Dot Nanocomposites by Reactive Inkjet Printing. Small. 2015; 11:1649–1654. [PubMed: 25641755]

23. Kim BH, Onses MS, Lim JB, Nam S, Oh N, Kim H, Yu KJ, Lee JW, Kim JH, Kang SK, Lee CH, Lee J, Shin JH, Kim NH, Leal C, Shim M, Rogers JA. High-Resolution Patterns of Quantum Dots Formed by Electrohydrodynamic Jet Printing for Light-Emitting Diodes. Nano Lett. 2015; 15:969–973. [PubMed: 25584701]
24. Shirasaki Y, Supran GJ, Bawendi MG, Bulović V. Emergence of Colloidal Quantum-Dot Light-Emitting Technologies. Nat Photonics. 2013; 7:13–23.
25. Koh, Wk, Saudari, SR., Fafarman, AT., Kagan, CR., Murray, CB. Thiocyanate-Capped Pbs Nanocubes: Ambipolar Transport Enables Quantum Dot Based Circuits on a Flexible Substrate. Nano Lett. 2011; 11:4764–4767. [PubMed: 22011060]
26. Meng C, Xiao Y, Wang P, Zhang L, Liu Y, Tong L. Quantum-Dot-Doped Polymer Nanofibers for Optical Sensing. Adv Mater. 2011; 23:3770–3774. [PubMed: 21766349]
27. Yu WW, Chang E, Falkner JC, Zhang J, Ali-Somali AM, Sayes CM, Jones J, Drezek R, Colvin VL. Forming Biocompatible and Non-Aggregated Nanocrystals in Water Using Amphiphilic Polymers. J Am Chem Soc. 2007; 129:2871–2879. [PubMed: 17309256]
28. Li JJ, Wang YA, Guo W, Keay JC, Mishima TD, Johnson MB, Peng X. Large-Scale Synthesis of Nearly Monodisperse CdSe/CdS Core/Shell Nanocrystals Using Air-Stable Reagents Via Successive Ion Layer Adsorption and Reaction. J Am Chem Soc. 2003; 125:12567–12575. [PubMed: 14531702]
29. Yu WW, Qu L, Guo W, Peng X. Experimental Determination of the Extinction Coefficient of CdTe, CdSe and CdS Nanocrystals. Chem Mater. 2003; 15:2854–2860.
30. Yu WW, Qu L, Guo W, Peng X. Experimental Determination of the Extinction Coefficient of CdTe, CdSe and CdS Nanocrystals: Correction. Chem Mater. 2004; 16:560.
31. Neumann O, Urban AS, Day J, Lal S, Nordlander P, Halas NJ. Solar Vapor Generation Enabled by Nanoparticles. ACS Nano. 2013; 7:42–49. [PubMed: 23157159]
32. Fang ZY, Zhen YR, Neumann O, Polman A, de Abajo FJG, Nordlander P, Halas NJ. Evolution of Light-Induced Vapor Generation at a Liquid-Immersed Metallic Nanoparticle. Nano Lett. 2013; 13:1736–1742. [PubMed: 23517407]
33. Roxworthy BJ, Ko KD, Kumar A, Fung KH, Chow EKC, Liu GL, Fang NX, Toussaint KC. Application of Plasmonic Bowtie Nanoantenna Arrays for Optical Trapping, Stacking, and Sorting. Nano Lett. 2012; 12:796–801. [PubMed: 22208881]
34. Lin L, Peng XL, Mao ZM, Li W, Yogeesh MN, Rajeeva BB, Perillo EP, Dunn AK, Akinwande D, Zheng YB. Bubble-Pen Lithography. Nano Lett. 2016; 16:701–708. [PubMed: 26678845]
35. Zhao C, Xie YL, Mao ZM, Zhao YH, Rufo J, Yang SK, Guo F, Mai JD, Huang TJ. Theory and Experiment on Particle Trapping and Manipulation Via Optothermally Generated Bubbles. Lab Chip. 2014; 14:384–391. [PubMed: 24276624]
36. Zheng Y, Liu H, Wang Y, Zhu C, Wang SM, Cao JX, Zhu SN. Accumulating Microparticles and Direct-Writing Micro-patterns Using a Continuous-Wave Laser-Induced Vapor Bubble. Lab Chip. 2011; 11:3816–3820. [PubMed: 21956638]
37. Fujii S, Kanaizuka K, Toyabe S, Kobayashi K, Muneyuki E, Haga M. Fabrication and Placement of a Ring Structure of Nanoparticles by a Laser-Induced Micronanobubble on a Gold Surface. Langmuir. 2011; 27:8605–8610. [PubMed: 21678969]
38. Xie Y, Zhao CL. Optothermally Generated Surface Bubble and Its Applications. Nanoscale, in press. 2017 10.1039/C7NR01360D.
39. Baffou G, Berto P, Urena EB, Quidant R, Monneret S, Polleux J, Rigneault H. Photoinduced Heating of Nanoparticle Arrays. ACS Nano. 2013; 7:6478–6488. [PubMed: 23895209]
40. Baffou G, Quidant R, de Abajo FJG. Nanoscale Control of Optical Heating in Complex Plasmonic Systems. ACS Nano. 2010; 4:709–716. [PubMed: 20055439]
41. Liu X, Bao L, Dipalo M, De Angelis F, Zhang XH. Formation and Dissolution of Microbubbles on Highly-Ordered Plasmonic Nanopillar Arrays. Sci Rep. 2015; 5 No. 18515.
42. Lohse D, Zhang XH. Surface Nanobubbles and Nano-droplets. Rev Mod Phys. 2015; 87:981–1035.
43. Baffou G, Polleux J, Rigneault H, Monneret S. Super-Heating and Micro-Bubble Generation around Plasmonic Nano-particles under CW Illumination. J Phys Chem C. 2014; 118:4890–4898.

44. Dalvi SV, Joshi JR. Modeling of Microbubble Dissolution in Aqueous Medium. J Colloid Interface Sci. 2015; 437:259–269. [PubMed: 25441359]

45. Eisfeld A, Briggs JS. Absorption Spectra of Quantum Aggregates Interacting Via Long-Range Forces. Phys Rev Lett. 2006; 96 No. 113003.

46. Markman A, Javidi B, Tehranipoor M. Photon-Counting Security Tagging and Verification Using Optically Encoded QR Codes. IEEE Photonics J. 2014; 6:1–9.

47. Kim BH, Nam S, Oh N, Cho SY, Yu KJ, Lee CH, Zhang JQ, Deshpande K, Trefonas P, Kim JH, Lee J, Shin JH, Yu Y, Lim JB, Won SM, Cho YK, Kim NH, Seo KJ, Lee H, Kim TI, Shim M, Rogers JA. Multilayer Transfer Printing for Pixelated, Multicolor Quantum Dot Light-Emitting Diodes. ACS Nano. 2016; 10:4920–4925. [PubMed: 27078621]

48. Meitl MA, Zhu ZT, Kumar V, Lee KJ, Feng X, Huang YY, Adesida I, Nuzzo RG, Rogers JA. Transfer Printing by Kinetic Control of Adhesion to an Elastomeric Stamp. Nat Mater. 2006; 5:33–38.

49. McHale JP, Garimella SV. Bubble Nucleation Characteristics in Pool Boiling of a Wetting Liquid on Smooth and Rough Surfaces. Int J Multiphase Flow. 2010; 36:249–260.

50. Kimura J, Uematsu T, Maenosono S, Yamaguchi Y. Photoinduced Fluorescence Enhancement in Cdse/Zns Quantum Dot Submonolayers Sandwiched between Insulating Layers: Influence of Dot Proximity. J Phys Chem B. 2004; 108:13258–13264.

51. Shcherbatyuk GV, Inman RH, Ghosh S. Anomalous Photo-Induced Spectral Changes in Cdse/Zns Quantum Dots. J Appl Phys. 2011; 110 No. 053518.

52. Rajeeva BB, Hernandez DS, Wang MS, Perillo E, Lin LH, Scarabelli L, Pingali B, Liz-Marzan LM, Dunn AK, Shear JB, Zheng YB. Regioselective Localization and Tracking of Biomolecules on Single Gold Nanoparticles. Adv Sci. 2015; 2 No. 1500232.

53. Hoang TB, Akselrod GM, Argyropoulos C, Huang JN, Smith DR, Mikkelsen MH. Ultrafast Spontaneous Emission Source Using Plasmonic Nanoantennas. Nat Commun. 2015; 6:7788. [PubMed: 26212857]

54. Chen J, Chan YH, Yang TL, Wark SE, Son DH, Batteas JD. Spatially Selective sOptical Tuning of Quantum Dot Thin Film Luminescence. J Am Chem Soc. 2009; 131:18204–18205. [PubMed: 20028145]

55. Zhang L, Chen C, Li W, Gao G, Gong P, Cai L. Living Cell Multilifetime Encoding Based on Lifetime-Tunable Lattice-Strained Quantum Dots. ACS Appl Mater Interfaces. 2016; 8:13187–13191. [PubMed: 27192191]

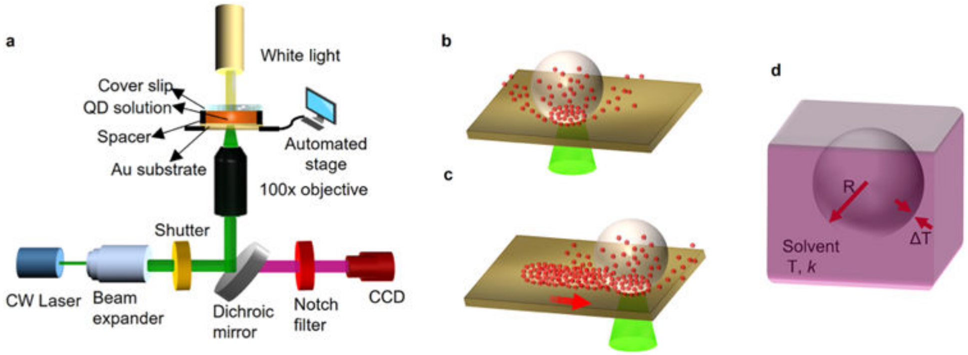

Figure 1.

Working principle of BP of QDs on plasmonic substrates. (a) Schematic of the optical setup for BP. (b) Schematic showing the QDs being trapped toward the bubble generated on the substrate and the eventual immobilization of QDs on the substrate. (c) Illustration of the QDs immobilized along the path traversed by the laser beam to create patterns of QDs on the substrate. (d) Schematic illustration of the different parameters that affect the outward heat flux and the bubble generation. T, solvent temperature; k, solvent thermal conductivity; R, radius of the bubble; ΔT, temperature difference across bubble surface.

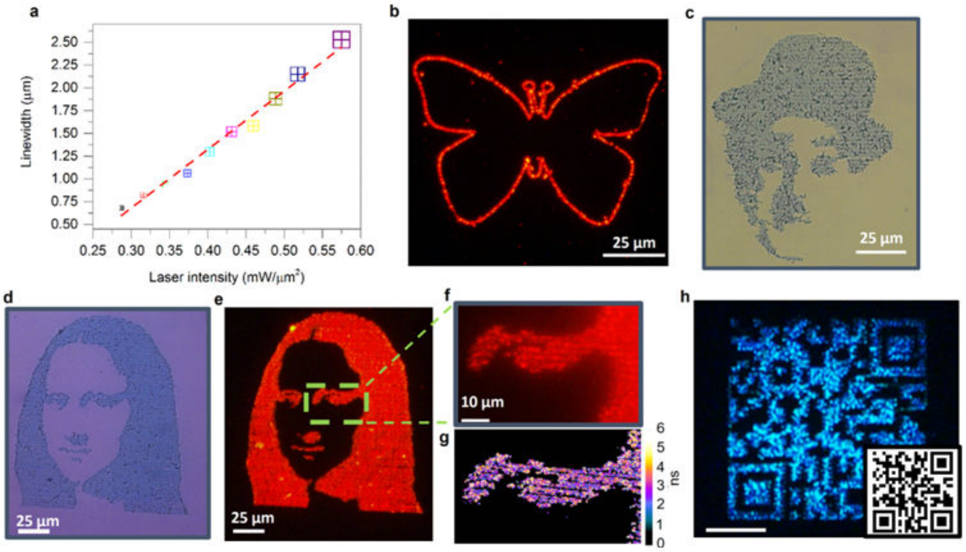

Figure 2.

Versatile BP capabilities: (a) Plot of pattern line width vs incident laser intensity. The linear fitting shows the on-demand capability of tuning the patterning dimensions by the laser power. (b) BP of red QDs into a contour of a butterfly, as shown in fluorescence image. The line width is 1 μm. (c) Bright-field image of a Charlie Chaplin pattern of QDs via raster scanning in BP. The overall size is 120 μm × 90 μm with 1 μm line space. (d, e) Bright-field and fluorescence images (tetramethylrhodamine isothiocyanate filter set) of Mona Lisa printed with red QDs using a raster scanning approach. The size of the complete image is 150 μm × 90 μm. (f) Magnified fluorescence image depicting the high-resolution patterning capability of BP. (g) FLIM of the QDs showing high-density uniform patterning capability of BP. (h) Fabrication of a microscale (80 μm × 80 μm) QR code with blue QDs printed via raster scanning. The scale bar is 25 μm.

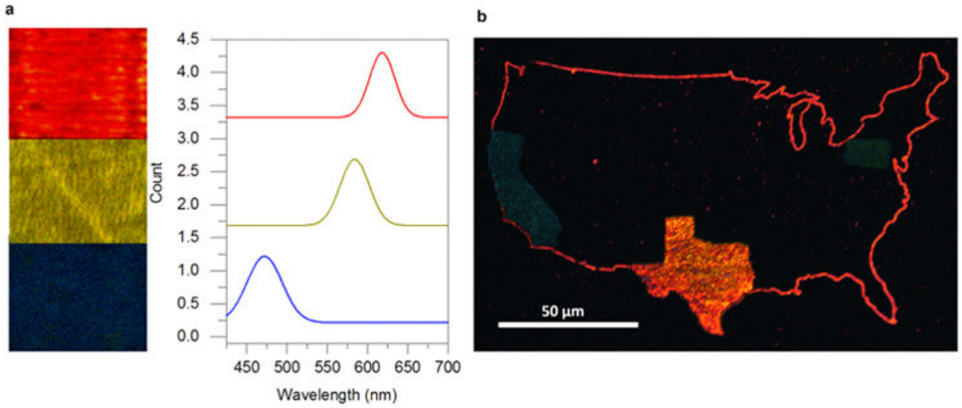

Figure 3.

Toward multicolor QD printing: (a) (Left) Fluorescence images of bubble-printed red, yellow, and blue QDs into three patterns. (Right) Corresponding fluorescence spectra of the three patterns depicting emission peaks from blue to red. (b) Integration of multiple QDs on a single substrate using multistep BP. The example is a U.S. map with the states of Texas, California, and Pennsylvania printed with different QDs. The size of the map is 120 μm × 200 μm, and each state is fabricated via raster scanning with a 1 μm line space.

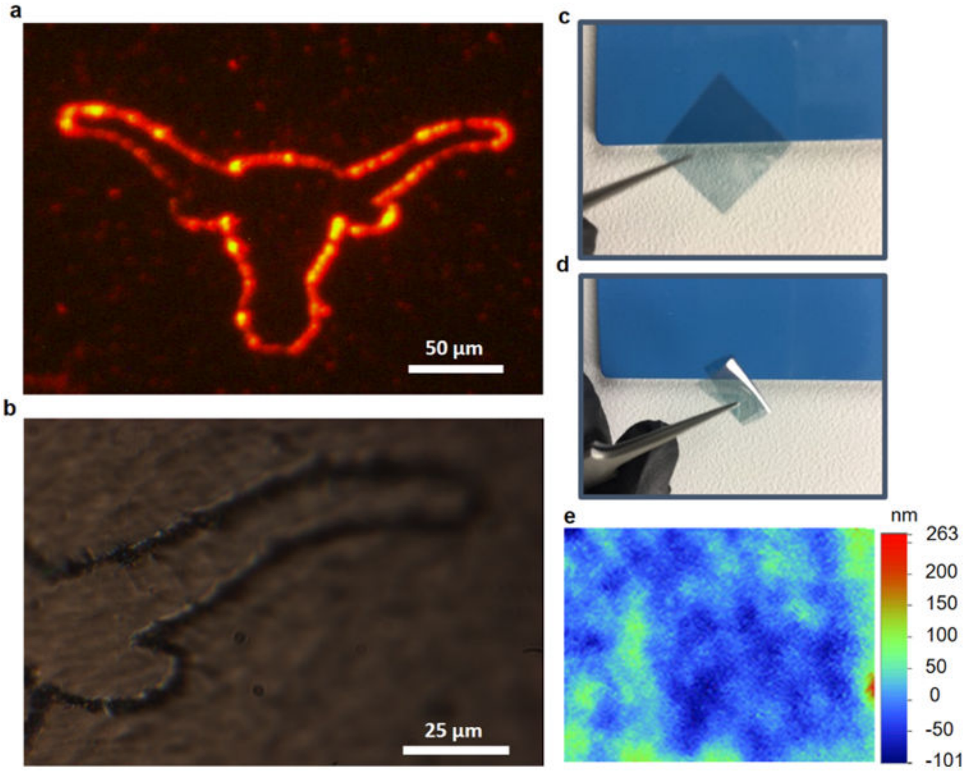

Figure 4.

BP of QDs on a flexible substrate: (a) Fluorescence image of the longhorn pattern printed with red QDs over a PET film obtained using TRITC filter set. (b) Bright-field image of the printed QDs with the PET film in the bent state. The strong adhesion of QDs to the substrate ensures that the high integrity of the pattern is maintained after the mechanical bending. (c, d) Optical images of the PET film under the original and bent states, respectively. (e) Optical profilometer image (Wyco 9100) of the PET film showing an RMS roughness of 35 nm.

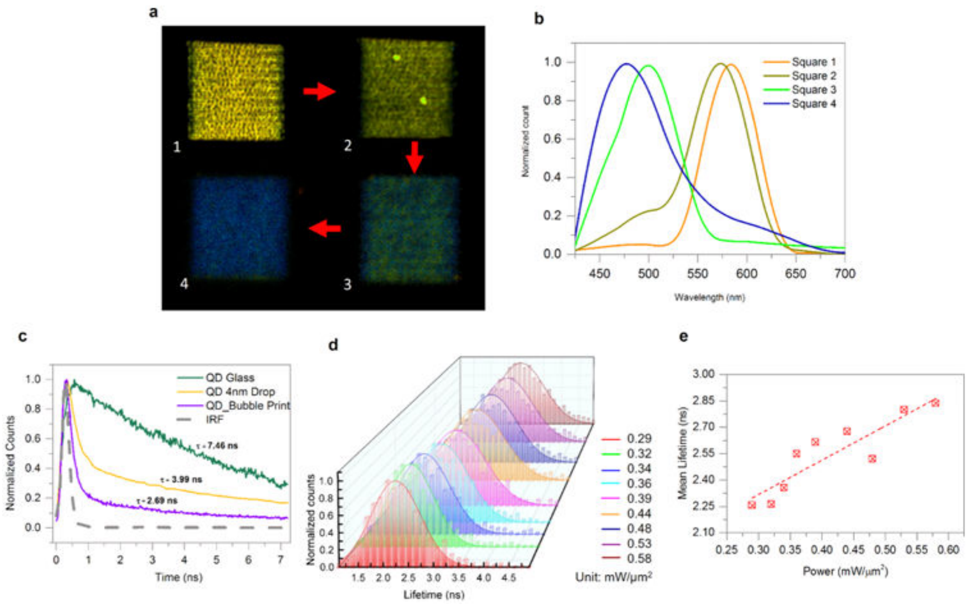

Figure 5.

Modification of fluorescence wavelengths and dynamics of patterned QDs: (a) Merged fluorescence image of yellow QDs patterned in four squares by variable BP parameters. The optical power, stage-translation speed, waiting time between the neighboring lines, and line spacing for the squares 1–4: (i) 0.52 mW/μm^2, 1000 μm/s, 500 ms, and 1 μm; (ii) 0.54 mW/μm^2, 500 μm/s, 600 ms, and 1 μm; (iii) 0.56 mW/μm^2, 100 μm/s, 800 ms, and 1 μm; and (iv) 0.58 mW/μm^2, 100 μm/s, 1 s, and 0.5 μm. Scale bar: 10 μm. (b) Fluorescence spectra from the four squares in (a). (c) Time-correlated fluorescence of red QDs: (i) drop-casted on glass, (ii) drop-casted on plasmonic substrate, and (iii) bubble-printed on plasmonic substrate. The lifetime decreases from 7.46 ns (QDs on glass) to 2.69 ns (QDs printed on plasmonic substrate). (d) Fluorescence lifetime modification by tuning the optical power in BP. See Figure S12 for details on the histogram. (e) Plot of the mean lifetime vs optical power in BP. The mean lifetime increases from 2.26 to 2.84 ns with an increase of optical power in BP.